

Thermal Emission and Tidal Heating of the Heavy and Eccentric Planet XO-3b

Pavel Machalek^{1,2}, Tom Greene¹, Peter R. McCullough³, Adam Burrows⁴,
Christopher J. Burke⁵, Joseph L. Hora⁵, Christopher M. Johns-Krull⁶, Drake L. Deming⁷

pavel.machalek@nasa.gov

ABSTRACT

We determined the flux ratios of the heavy and eccentric planet XO-3b to its parent star in the four IRAC bands of the Spitzer Space Telescope: $0.101\% \pm 0.004\%$ at 3.6 micron; $0.143\% \pm 0.006\%$ at 4.5 micron; $0.134\% \pm 0.049\%$ at 5.8 micron and $0.150\% \pm 0.036\%$ at 8.0 micron. The flux ratios are within $[-2.2, 0.3, -0.8, -1.7]$ - σ of the model of XO-3b with a thermally inverted stratosphere in the 3.6 micron, 4.5 micron, 5.8 micron and 8.0 micron channels, respectively. XO-3b has a high illumination from its parent star ($F_p \sim (1.9 - 4.2) \times 10^9$ ergs $\text{cm}^{-2} \text{s}^{-1}$) and is thus expected to have a thermal inversion, which we indeed observe. When combined with existing data for other planets, the correlation between the presence of an atmospheric temperature inversion and the substellar flux is insufficient to explain why some high insolation planets like TrES-3 do not have stratospheric inversions and some low insolation planets like XO-1b do have inversions. Secondary factors such as sulfur chemistry, atmospheric metallicity, amounts of macroscopic mixing in the stratosphere or even dynamical weather effects likely play a role. Using the secondary eclipse timing centroids we determined the orbital eccentricity of XO-3b as $e = 0.277 \pm 0.009$. The model radius-age trajectories for XO-3b imply that at least some amount of tidal-heating is

¹NASA Ames Research Center, MS 245-6, Moffett Field, CA 94035

²Bay Area Environmental Research Institute, 560 Third St West, Sonoma, CA 95476

³Space Telescope Science Institute, 3700 San Martin Dr., Baltimore MD 21218

⁴Department of Astrophysical Sciences, Princeton University, Princeton, NJ 08544

⁵Harvard-Smithsonian Center for Astrophysics, 60 Garden St., Cambridge, MA 02138

⁶Department of Physics and Astronomy, Rice University, 6100 Main Street, MS-108, Houston, TX 77005

⁷Planetary Systems Laboratory, NASA/GSFC, Code 693.0, Greenbelt, MD 20771

required to inflate the radius of XO-3b, and the tidal heating parameter of the planet is constrained to $Q_p \lesssim 10^6$.

Subject headings: stars:individual(XO-3) — binaries:eclipsing — infrared:stars — planetary systems

1. Introduction

The study of hot Jupiter atmospheres is maturing. In particular, low resolution spectra and broadband spectral energy distributions have been assembled from high precision photometry of Hot-Jupiter’s day and night sides using the Spitzer Space Telescope’s InfraRed Array Camera (IRAC) (Knutson et al. 2008, 2009b; Tinetti et al. 2007; Charbonneau et al. 2008; Machalek et al. 2008, 2009; O’Donovan et al. 2009; Désert et al. 2009; Todorov et al. 2010; Fressin et al. 2009; Christiansen et al. 2009), Infrared Spectrograph (IRS) (Grillmair et al. 2008) and Multi Band Imaging Spectrometer (MIPS) (Knutson et al. 2009a) as well the Hubble Space Telescope (Swain et al. 2008a, 2009a,b).

Upper atmospheres of hot Jupiters are currently thought to be split into two classes depending on the stellar insolation at their substellar points: planets with substellar flux higher than $F_p \gtrsim 10^9 \text{ erg cm}^{-2} \text{ s}^{-1}$ should possess temperature inversions in their stratosphere as the intense stellar radiation is absorbed by upper atmospheric gaseous absorbing species (Hubeny et al. 2003; Burrows et al. 2008; Fortney et al. 2006, 2008; Spiegel et al. 2009). Planets with insolation fluxes $F_p \sim 0.5\text{-}1.0 \times 10^9 \text{ ergs cm}^{-2} \text{ s}^{-1}$ like XO-2b, HAT-P-1, OGLE-TR-113, and WASP-2 are in a transition zone between atmospheres with or without a stratosphere. Secondary effects like sulfur chemistry and atmospheric metallicity (Zahnle et al. 2009), amounts of macroscopic mixing in the stratosphere (Spiegel et al. 2009) or even dynamical weather effects (Showman et al. 2009; Rauscher & Menou 2009) could determine the stratospheric temperature profiles of these transition planets.

XO-3b is a hot Jupiter with a high mass $M_p = 11.79 \pm 0.59 M_{Jup}$ (Winn et al. 2008; Johns-Krull et al. 2008), which is close to the deuterium burning limit and has one of the highest observed surface gravities, $g = 209 \text{ m s}^{-2}$ amongst the known transiting planets. Its 3.1915239 day long orbit around the parent star XO-3 (spectral type F5V, $d = 260 \pm 23 \text{ pc}$, Johns-Krull et al. (2008)) has significant eccentricity $e = 0.287 \pm 0.005$ (Hébrard et al. 2008)), which causes stellar irradiance to vary three-fold over the entire orbit and causes the secondary eclipse to shift in time from half-phase.

Furthermore Liu et al. (2008) estimated the amount of tidal energy dissipation rate

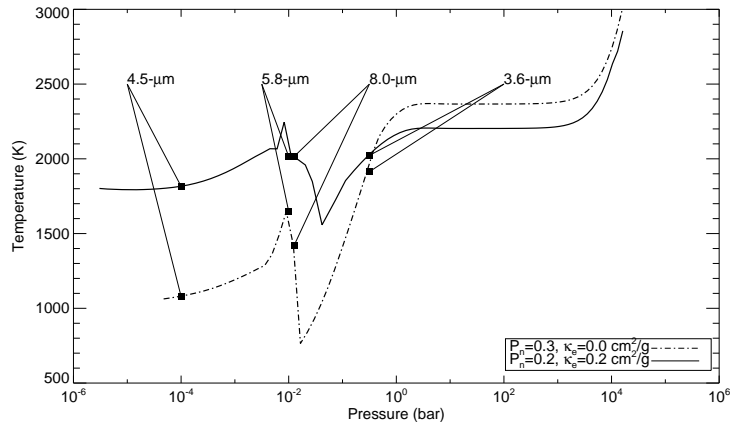


Fig. 1.— (top) Temperature / Pressure profiles for the atmosphere of XO-3b following the methodology of Burrows et al. (2007b, 2008); Spiegel et al. (2009) for heat redistribution parameter $P_n=0.3$ with no upper atmospheric optical absorber (dot-dashed line) and a corresponding model with a uniform upper atmospheric absorber (solid line) (absorption coefficient $\kappa_e=0.2 \text{ cm}^2/\text{g}$ and heat re-distribution parameter $P_n=0.2$) with depths corresponding to emission in the IRAC channels denoted. Both Temperature/Pressure profiles are calculated for XO-3b orbital distance $a = 0.0454 \text{ AU}$ (Winn et al. 2008) and stellar insolation $F_p \sim 2.01 \times 10^9 \text{ ergs cm}^{-2} \text{ s}^{-1}$. See §3.2 for more details.

contributing to the inflated radius of XO-3b ($R_p = 1.217 \pm 0.073 R_{Jup}$; Winn et al. 2008) assuming the age of XO-3b $t = 2.82^{+0.58}_{-0.82} \text{ Gyr}$ (Winn et al. 2008). Liu et al. (2008) concluded that the radius-age relationship for XO-3b is consistent to within $1.0\text{-}\sigma$ with no internal heat source (i.e. no tidal heating) or tidal heating dissipation with dimensionless tidal heating parameter $Q_p \gtrsim 10^6$ as defined by Goldreich & Soter (1966). By determining the exact timing of the secondary eclipse in our 4 infrared light curves obtained with *Spitzer Space Telescope* IRAC we will refine the orbital eccentricity of XO-3b and constrain the amount of tidal heating (if any) responsible for inflating the planetary radius. In addition to its high mass and significant orbital eccentricity, XO-3b was also the first planet with detected and confirmed non-zero sky projection angle $\lambda = 37.3 \pm 3.7 \text{ deg}$ between the orbital axis and stellar rotation axis obtained from the Rossiter-McLaughlin effect (Hébrard et al. 2008; Winn et al. 2009), currently thought to be a result of planet-planet scattering (Nagasawa et al. 2008; Jurić & Tremaine 2008).

The substellar point flux at XO-3b is $F_p \sim (1.9 - 4.2) \times 10^9 \text{ ergs cm}^{-2} \text{ s}^{-1}$. The exact value depends on the adopted stellar and planetary mass and radius, which are still uncertain Liu et al. (2008), as well as the changing distance distance from the star due to an

eccentric orbit. However this range of substellar point flux is clearly consistent with a prominent thermal inversion in the stratosphere. Figure 1 shows Temperature- Pressure models of Burrows et al. (2007b, 2008); Spiegel et al. (2009) and the predicted thermal inversion in the stratosphere and the negative temperature gradient in the upper atmosphere of XO-3b.

By obtaining the light curve of XO-3b in the 4 IRAC (4-8 microns) channels on the *Spitzer Space Telescope* and determining the depth and timing of the secondary eclipse in multiple wavelengths, we will be able to constrain the upper atmospheric temperature structure of XO-3b, refine the orbital eccentricity of the planet from the secondary eclipse timing centroids and hence its tidal heating rate, which could be responsible for inflating the radius of XO-3b. The Cold Spitzer IRAC observations in this work will provide a firm observational and theoretical foothold on the properties of the XO-3b atmosphere during the secondary eclipse and serve as comparison for future full orbit observation of XO-3b with Warm Spitzer similar to previous extended duration phase curves of hot Jupiters (Knutson et al. 2007, 2009a,c; Laughlin et al. 2009). Since there is a strong water band near IRAC 5.8 micron, coverage in all four IRAC bands will test for transitions between water in emission and in absorption, which can not be observed with Warm Spitzer. Furthermore as Fig. 1 illustrates, there is a steep temperature gradient between depths corresponding to emission in IRAC 5.8/8.0 micron channels, which can be uniquely studied with Cold Spitzer or otherwise with JWST in the future. The 5.8 and 8.0 micron channel planet/star flux ratios will further be correlated with the 3.6/ 4.5 micron flux ratio to test the two signatures of stratospheres.

2. Observations & Data Analysis

The InfraRed Array Camera (IRAC; Fazio et al. 2004) has a field of view of $5.2' \times 5.2'$ in each of its four bands. Two adjacent fields are imaged in pairs (3.6 and 5.8 microns; 4.5 and 8.0 microns). The detector arrays each measure 256×256 pixels, with a pixel size of approximately $1.22'' \times 1.22''$. We closely repeat the data analysis of Machalek et al. (2008, 2009) with modifications and improvements mentioned in the text.

We have observed XO-3 system in all 4 channels in two separate Astronomical Observing Requests (AORs) in two different sessions: the 3.6 and 5.8 micron channels for 6.9 hours (with 2.9 hour long secondary eclipse) on UT 2009 March 17 (AOR 31618560) and the 4.5 and 8.0 micron channels for 6.9 hours on UT 2009 April 21 (AOR 31618816) with a 30-minute preflash on a bright uniform part of NGC1569. We used the full array 2s+2s/12s frame time in the stellar mode in which the 3.6 micron and 4.5 micron bands are exposed

for two consecutive 2s exposures while the 5.8 micron and 8.0 micron bands are integrating for 12s to prevent detector saturation.

The 4.5 micron and 8.0 micron time series has been preflashed with a bright uniform extended target to prevent the initial “ramp-up” effect (Charbonneau et al. 2005; Deming et al. 2005; Knutson et al. 2008; Machalek et al. 2008, 2009), consequently no data points were removed from the beginning of the time series. The 3.6 micron and 5.8 micron time series however were obtained with no pre-flashing and hence exhibit an initial charge build up which is consistently removed during our detector effect removal.

2.1. InSb Detectors

We have repeated our methodology from Machalek et al. (2009) by performing aperture photometry on the 3.6 micron and 4.5 micron time series with radii between 2.5 and 6.0 pixels. In order to test whether our secondary eclipse depths and centroid timings depend on aperture radius, we have repeated the entire data reduction for aperture radii between 2.5 and 6.0 pixels in 0.5 pixel increments and obtained consistent results for different apertures. We have improved our photometry pipeline by obtaining the stellar centroids from flux-weighted position of a 5×5 pixel square centered on the peak stellar pixel (method suggested by Sean Carrey, private communication). Since our starting point was the BCD images produced by the pipeline version 18.7, cosmic rays were already rejected. The heliocentric modified Julian date at Spitzer spacecraft position recorded in the header keyword “HMJD_OBS” did not necessitate our previous calculations of spacecraft positions (Machalek et al. 2008, 2009).

We have chosen the aperture radii based on the RMS of residuals after detector effects and the secondary eclipse were removed. We used an aperture of radius 3.0 pixels for the 3.6 micron time series of XO-3, which had an RMS 0.0034 for out of transit points after decorrelation. This is essentially Poisson noise limited, being only 1.01 higher than the predicted noise based on source brightness, detector read noise and gain. Similarly the 4.5 micron time series of XO-3 was obtained from 3.0 pixel radius aperture photometry which had the lowest RMS of 0.0049 which is 1.08 times higher than the predicted noise. The appropriate aperture corrections were applied to the photometry as specified by the Spitzer Data Handbook.

As is evident from Fig. 3, the 3.6 micron time series exhibits a prominent flux variation with magnitude of $\sim 0.8\%$, which is a well studied instrumental effect (Charbonneau et al. 2005; Morales-Calderón et al. 2006; Machalek et al. 2008; Knutson et al. 2009b; Machalek et al. 2009; Désert et al. 2009) due to sub-pixel sensitivity variations caused by spacecraft

position drift of 0.1 - 0.3 arcsec over a period of ~ 3000 seconds, which makes the star move on the pixel. The 4.5 micron time series, however, has negligible flux variations, probably due to a chance positioning on a pixel phase with a flat response curve (pixel reference: 126.46; 128.78). This pixel could be useful in planning for extended duration observations with Warm Spitzer. Désert et al. (2009) has noted a similar pixel with a flat response function at pixel coordinates [147.20; 198.25].

Our removal of the systematic effects and eclipse curve fitting closely follows the methodology of Machalek et al. (2009). The subpixel intensity variations in the 3.6 micron and 4.5 micron time series are detrended as a linear function of subpixel positions of the stellar centroid x , y , x^2 , y^2 , a linear function of time t , plus a constant for each of the two InSb channels:

$$I_{3.6micron} = 1.0 + b_1x + b_2y + b_3x^2 + b_4y^2 + b_5t, \quad (1)$$

$$I_{4.5micron} = 1.0 + b_1x + b_2y, \quad (2)$$

We tried adding higher order terms of x and y , a cross terms of $x \times y$, and a linear term linear in t to the 4.5 micron time series decorrelation. However, adding terms did not decrease the χ^2 or change the secondary eclipse depth or centroid timing in the 4.5 micron time series, so we chose only two degrees of freedom (Eq. 2) for the 4.5 micron time series decorrelation. Furthermore as can be seen from Fig. 2, the binned residuals in the decorrelated and fitted 4.5 micron light curve of XO-3 scale as $N^{-1/2}$, where N is the number of points per bin. Since the binning of the residuals scales as $N^{-1/2}$ we can conclude that negligible systematic errors remain in the decorrelated light curve.

We fit the secondary eclipse with the formalism of Mandel & Agol (2002) with no stellar limb darkening and adopt the stellar and planetary parameters of Winn et al. (2008):

$R_\star = 1.38_{-0.08}^{+0.08} R_\odot$, $M_p = 11.79_{-0.59}^{+0.59} M_{Jup}$, $R_p = 1.22_{-0.07}^{+0.07} R_{Jup}$ ¹, $i = 84.20_{-0.54}^{+0.54}$ degrees, and $a = 0.0454 \pm 0.0008$ AU with ephemeris:

$$T_c(E) = 2,454,449.86816(HJD) + E(3.1915239 \text{ days}). \quad (3)$$

We fit the 5 baseline parameters of Eq. 1 and the 2 baseline fitting parameters Eq. 2 concurrently with the secondary eclipse depth ΔF and the phase of the eclipse centroid Φ

¹ $R_{Jup} = 71,492$ km.

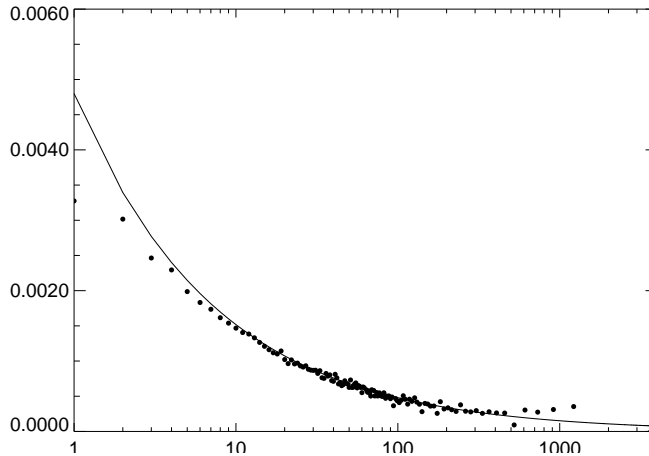


Fig. 2.— Root mean square of binned light curve points after detector removal and secondary eclipse fitting for the 4.5 micron photometry of XO-3 vs. the number of points per bin. The sub-pixel phase sensitivity variations were removed using Eq. 2. The solid line is proportional to the number of residual points per bin $N^{-1/2}$.

for a total of 7 and 4 fitting parameters, respectively. This was done to properly account for the way in which systematic effects removal affects the secondary eclipse fitting. The best parameter solutions were obtained by using a Monte Carlo Markov Chain (MCMC) with 10^5 iterations (Gregory 2005; Markwardt 2009) with ratio of jumps between 20-40 %. The best fit parameter values were obtained by discarding the first 20% of the iterations to prevent initial conditions from influencing the results and adopting the median of the distribution of each parameter as the best fit value. These values are reported in Table 1 with errors obtained from symmetric 66.8% contours around the median of the posterior probability distribution of the MCMC runs. The decorrelated best-fit light curves are depicted in Fig. 4 binned in 3.5 minute intervals. Note, however, that all our analysis is performed on the unbinned data.

We find that the XO-3 3.6 micron time series shows a linear flux increase with a slope of $b_4 = 0.015\% \pm 0.002\%$ per hour which is consistently removed from our photometry, but inconsistent with the slope of XO-2 at 3.6 micron of $b_4 = -0.011\% \pm 0.005\%$ per hour (Machalek et al. 2009). This flux decrease has been attributed by Machalek et al. (2009) and Knutson et al. (2009b) to an instrumental effect on the In:Sb detectors. When we added a linear time term b_3t to the decorrelation of the 4.5 micron time series of XO-3 in Eq. 2, its value was consistent with zero. Thus we omitted a linear time term b_3t from the final analysis.

2.2. Si:As Detectors

The 5.8 micron and 8.0 micron time series is recorded with Si:As detectors, which have a different set of systematic effects from the 3.6 micron and 4.5 micron InSb detectors. We have performed aperture photometry on the 5.8 micron and 8.0 micron images with aperture radii ranging from 3.0 to 6.0 pixels, choosing the aperture radius with the lowest RMS of the residuals after systematic effects and the secondary eclipse were removed. This resulted in an aperture of radius 3.5 pixels for the 5.8 micron time series with a detrended RMS of 0.0055 (42% higher than Poisson noise) and an aperture radius of 4.5 pixels for the 8.0 micron time series with a detrended RMS of 0.0049 (60% higher than Poisson noise). No points were removed from the beginning of either the 5.8 micron or 8.0 micron time series.

A well studied instrumental effect of the Si:As arrays is the gain variations of individual pixels over time, which result in flux decrease/increase in the light curve (e.g. Deming et al. 2005; Knutson et al. 2007, 2008; Machalek et al. 2008; Désert et al. 2009), quite unlike the pixel position dependent flux effect in the InSb 3.6 micron and 4.5 micron arrays. Machalek et al. (2009) and Laughlin et al. (2009) have reported that the gain variations in the 5.8 micron and 8.0 micron channels and resultant flux trends in the light curves differ for the two components of a binary star, which have the same brightness and similar colors, suggesting that relative placement of the stellar centroid with respect to the edges of the pixels determines the Si:As detector pixel response. The gain variations can be clearly seen in the 5.8 micron and 8.0 micron light series in Fig. 3: a nonlinear decrease in brightness in the 5.8 micron light series and a nonlinear flux increase in the 8.0 micron time series.

To remove the nonlinear flux variation inherent to the Si:As detector, we fit the secondary eclipse depth ΔF along with the eclipse centroid phase Φ concurrently with the 3 “ramp” decorrelation coefficients as follows:

$$I_{model} = a_1 + a_2 \times \ln(\Delta t + 0.05) + a_3 \times \ln(\Delta t + 0.05)^2 \quad (4)$$

where I_{model} is the normalized model flux and Δt is the time in days since the beginning of the integration (constant of +0.05 inserted to avoid singularity at $\Delta t=0$). We fit the 5 parameters (2 for the eclipse and 3 for the “ramp” in Eq. 4) for the 5.8 micron and 8.0 micron time series concurrently using 10^5 MCMC runs with errors adopted as the 66.8 % contours around the median of the posterior distribution of the MCMC runs for each parameter. To ensure that our results are not dependent on the aperture radius we have repeated the MCMC runs for all aperture radii between 3.0 and 6.0 pixels in 0.5 pixel in-

crements and found the timing centroids to be consistent. The secondary eclipse depths were, however, found to vary by about $1\text{-}\sigma$ for photometry with aperture radii between 3.0 and 6.0 pixels. Hence to be conservative, as stated above, we have adopted the secondary eclipse depths from the aperture photometry with the lowest RMS of residuals after eclipse removal. These aperture radii were 3.5 pixels for the 5.8 micron time series and 4.5 pixels for the 8.0 micron time series. We adopted uncertainties as the upper and lower envelope of the eclipse depths with their uncertainties for photometry with aperture radii between 3.0 and 6.0 pixels. Note, however, that these large, conservative uncertainties of the 5.8 micron and 8.0 micron eclipse depths ($\Delta F_{5.8 \text{ micron}} = 0.134\% \pm 0.049\%$ and $\Delta F_{8.0 \text{ micron}} = 0.150\% \pm 0.036\%$) still allow us to distinguish between the two models for the upper atmospheric temperature structure of XO-3b (see Fig. 5). The final results are reported in Table 1, and the decorrelated time series was binned in 3.5-minute bins for viewing clarity in Fig. 4.

3. Discussion

The IR light curves presented in this work allow for the determination of the exact timing of the secondary eclipse centroid such that the orbital eccentricity can be refined more accurately than from the radial velocity (RV) curve. The temperature structure of the upper atmosphere of XO-3b can also be determined from the light curves by comparing the secondary eclipse depths (i.e. the planet/star contrast ratios) to atmospheric models. A refined eccentricity determines the rate of tidal heating of the planet and can help explain the inflated radius of XO-3b.

3.1. Tidal heating rate and the radius of the planet

A subset of transiting extrasolar giant planets (EGPs) have radii larger than standard models can accommodate (Guillot et al. 1996; Bodenheimer et al. 2001, 2003; Chabrier et al. 2004; Ibgui & Burrows 2009). Numerous explanations have been suggested as sources of the inflated radii of EGPs (see Fortney & Nettelmann (2009) for a review). Working in opposition to any inflation mechanism, heavy-element inner cores lead to smaller planetary radii compared to pure H/He objects (Burrows et al. 2007a; Fortney et al. 2007; Baraffe et al. 2008). Tidal inflation has been a popular explanation, as the dissipation of orbital energy into the inner regions of a planet can lead to inflated radii (Bodenheimer et al. 2001, 2003; Liu et al. 2008). Radius-age trajectories for extra-solar giant planets (EGPs) are presented by Liu et al. (2008) to explain the inflated radius of several planets, including XO-3b, which is larger than theoretical predictions.

Liu et al. (2008) have investigated the radius of XO-3b as a function of planetary age t , planetary radius R_p , planetary mass M_p , orbital eccentricity e , planetary metallicity $[\text{Fe}/\text{H}]$, and tidal heating parameter Q_p . They conclude that for the parameters adopted from the photometric follow-up of XO-3b by Winn et al. (2008), which are used in our study (see §2.1), the radius $R_p = 1.22^{+0.07}_{-0.07} R_{Jup}$ adopted by Winn et al. (2008) is consistent within 1-sigma to either no internal heat source or tidal energy dissipation with tidal heating parameter $Q_p \gtrsim 10^{6.0}$. This is the heating parameter for the adopted eccentricity based upon RV measurements from Winn et al. (2008), $e = 0.260 \pm 0.017$. We have also adopted these parameters of Winn et al. (2008) up to this point in this study (see §2.1).

We refine the eccentricity e of XO-3b using the weighted average of the secondary eclipse timing centroids from Table 1 using the displacement from half orbital phase as a measurement of eccentricity (e.g. Kopal (1959) Eq. 9.23):

$$2\pi\Phi \simeq \pi + 2e \times \cos(\omega)(1 + \csc^2(i)) + \dots \quad (5)$$

where e is the eccentricity, Φ is the orbital phase of the time centroid of the secondary eclipse, ω is the longitude of periastron, and i is the planetary orbit inclination. Using argument of pericenter $\omega = 345.8 \text{ deg} \pm 7.3 \text{ deg}$ and inclination $i = 84.20 \text{ deg} \pm 0.54 \text{ deg}$ from Winn et al. (2008), we derive a refined eccentricity of the XO-3b system from our secondary eclipse timings:

$$e = 0.277 \pm 0.009 \quad (6)$$

with uncertainties formally propagated through Eq. 5. Taken individually the March 2009 secondary eclipse phase centroids from Table 1 imply an eccentricity of 0.278 ± 0.010 and the April 2009 secondary eclipse phase centroids imply eccentricity of 0.276 ± 0.009 , which are consistent with each other. The intriguing possibility of eccentricity changing on a timescale of months will be further studied during the Warm Spitzer mission phase observations of XO-3b in spring 2010, when both the transit and secondary eclipse will be observed.

The refined value of XO-3b eccentricity $e = 0.277 \pm 0.009$ is $1.0\text{-}\sigma$ higher than the Winn et al. (2008); Johns-Krull et al. (2008) eccentricity $e = 0.260 \pm 0.017$. It is also $2.0\text{-}\sigma$ lower than the radial velocity derived eccentricity $e = 0.287 \pm 0.005$, Hébrard et al. (2008). The tidal heating of XO-3b, which is a strong function of eccentricity, can inflate the radius of

the planet. To estimate the relevance of tidal heating to the energy budget of XO-3b, we evaluate the ratio of the tidal energy dissipation rate to the insolation rate from the parent star (Liu et al. 2008):

$$\frac{\dot{E}_{tide}}{\dot{E}_{insolation}} = \frac{GM_*\mu f(e)}{\pi F_p R_p^2 a \tau_{circ}} \quad (7)$$

$$\sim 6.9 \times 10^{-5} \left(\frac{e}{0.01}\right)^2 \left[\frac{f(e)}{e^2}\right] \left(\frac{Q_p}{10^5}\right)^{-1} \left(\frac{M_*}{M_\odot}\right)^{5/2} \left(\frac{R_p}{R_j}\right)^3 \left(\frac{a}{0.05AU}\right)^{-15/2} \left(\frac{F_p}{10^9 \text{ ergs cm}^{-2} \text{ s}^{-1}}\right)^{-1}$$

where \dot{E}_{tide} is the tidal energy dissipation within the planet’s rest frame, $\dot{E}_{insolation}$ is the insolation rate of the planet $\dot{E}_{insolation} = \pi R_p^2 F_p$, where R_p is the radius of the planet; F_p is the stellar flux at the planet’s substellar point; μ is the reduced mass $\mu \equiv \frac{M_* M_{planet}}{M_* + M_{planet}}$; τ is the circularization timescale as defined by Liu et al. (2008); e is orbital eccentricity; $f(e)$ is a function of eccentricity $f(e) \equiv \frac{2}{7}(h_3(e) - 2h_4(e) + h_5(e))$. The terms of $f(e)$ follow from the expansion of the expression of the tidal energy dissipation within the planet’s rest frame in terms of the Runge-Lenz vector (see Gu et al. (2003) for more details) with $h_3(e) = (1 + 3e^2 + \frac{3}{8}e^4)(1 - e^2)^{-9/2}$; $h_4(e) = (1 + \frac{15}{2}e^2 + \frac{45}{8}e^4 + \frac{5}{16}e^6)(1 - e^2)^{-6}$ and $h_5(e) = (1 + \frac{31}{2}e^2 + \frac{255}{8}e^4 + \frac{185}{16}e^6 + \frac{25}{64}e^8)(1 - e^2)^{-15/2}$. Q_p is the dimensionless tidal dissipation parameter of the planet (Goldreich & Soter 1966); M_* is the mass of the star in solar units; R_p is the radius of the planet and a is the semi-major axis.

Using Eq.7 we estimate the ratio of tidal heating dissipation rate to the insolation rate of XO-3b to be $\frac{\dot{E}_{tide}}{\dot{E}_{insolation}}|_{e=0.260} \sim 0.43$ given the Winn et al. (2008) planetary and stellar parameters: $M_* = 1.213 \pm 0.066 M_\odot$, $M_p = 11.79_{-0.59}^{+0.59} M_{Jup}$, $R_p = 1.22_{-0.07}^{+0.07} R_{Jup}$, $a = 0.0454 \pm 0.0008$ AU, $F_p = 1.93 \times 10^9 \text{ erg cm}^{-2} \text{ s}^{-1}$, planetary tidal dissipation parameter $Q_p = 10^5$ and radial-velocity derived eccentricity of $e = 0.260 \pm 0.017$.

Our study refines the eccentricity of XO-3b $e = 0.277 \pm 0.009$, which yields a ratio $\frac{\dot{E}_{tide}}{\dot{E}_{insolation}}|_{e=0.277} \sim 0.56$ i.e. a 29% increase in the tidal dissipation rate over the lower eccentricity when all other parameters are unchanged. Figure 2 of Liu et al. (2008) would suggest that if the age of XO-3b is currently estimated to be $t = 2.82_{-0.82}^{+0.58}$ GYr (Winn et al. 2008) and for solar metallicity, the increased tidal heating rate from our work would require a lowered tidal dissipation parameter $Q_p \lesssim 10^6$. Furthermore the radius-age trajectory for XO-3b with $M_p = 11.79_{-0.59}^{+0.59} M_{Jup}$, $R_p = 1.22_{-0.07}^{+0.07} R_{Jup}$ and the refined eccentricity $e = 0.277 \pm 0.009$ is inconsistent with no tidal heating depicted by infinite tidal heating parameter $Q = \infty$. An important caveat to our radius interpretations for XO-3b is that we assume that tidal heating is the only radius inflation mechanism. Furthermore, the distance to XO-3b is still very uncertain ($d = 260 \pm 23$ pc). Also, the discovery paper by Johns-Krull et al. (2008) and the photometric followup by Winn et al. (2008) disagree on the mass of XO-3b

by 10% and more than 50% on the radius. Detailed radius-age determinations for XO-3b and its tidal heating history will thus need a parallax determination, which is in progress (Johns-Krull 2008). Furthermore given the rudimentary nature of the Q model of tides, the assumption that dissipation is all in the convective core, and without detailed knowledge of the real physics of tidal dissipation, our conclusions about tidal heating rates and inferred radii of XO-3b are preliminary.

In short, we have refined the orbital eccentricity of XO-3b using the secondary eclipse timings in the 4 IRAC channels to $e = 0.277 \pm 0.009$, which increases the rate of tidal heating of the planet by 29% over previous eccentricity estimates. Even in the absence of an accurate parallax measurement, the radius-age trajectory of XO-3b (Fig.2 of Liu et al. 2008) seems to imply that at least some amount tidal heating must be responsible for the inflated radius of XO-3b.

3.2. Stratospheric temperature profile

The eclipse depths reported in Table 1 and depicted as filled squares in Fig. 5 show the spectral energy distribution of the upper atmosphere of XO-3b as a function of the flux ratio between XO-3b and its parent star XO-3. The flux ratio increases from the 3.6 micron to the 4.5 micron channels and stays constant within errors in the 5.8 micron and 8.0 micron channels. We compare the flux ratios (filled squares) to atmospheric models based on the methodology of Burrows et al. (2007b, 2008); Spiegel et al. (2009), which are depicted in Fig. 5 as a black solid line (and open squares as IRAC band averages) and a dot-dashed line with open circles as IRAC band averages.

The black solid line with open squares presents an atmospheric model with upper atmospheric temperature inversion induced by an extra absorber of uniform opacity of $\kappa_e = 0.2 \text{ cm}^2/\text{g}$ placed at optical wavelengths and placed high up in altitude at pressures below $P_0 = 30 \text{ mbars}$ in XO-3b's atmosphere. The model incorporates a heat re-distribution parameter of $P_n = [0.2]$, which corresponds to an atmosphere between the two extremes of no heat re-distribution ($P_n=0$) and full re-distribution ($P_n=0.5$) (see Burrows et al. (2008) for more details). The dot-dashed line with open circles as IRAC band averages corresponds to an atmospheric model with no extra upper atmospheric absorber and a heat re-distribution parameter of $P_n = [0.3]$.

Both atmospheric model are calculated for XO-3b's orbital distance $a = 0.0454 \text{ AU}$ (Winn et al. 2008) and stellar insolation $F_p \sim 2.01 \times 10^9 \text{ ergs cm}^{-2} \text{ s}^{-1}$, which ignores the dynamical atmospheric effects due to variable stellar insolation caused by XO-3b orbital eccentricity

$e = 0.277 \pm 0.009$. A full dynamical model for the atmosphere of XO-3b, which incorporates the time variable stellar insolation and the temporal adjustment of the atmosphere to the instantaneous irradiation (i.e. the radiative time constant), is beyond the scope of this paper. Full dynamical treatment of XO-3b’s atmosphere is planned for the dynamic weather observations of XO-3b during the Warm Spitzer mission in the spring of 2010 in the 3.6 micron and 4.5 micron IRAC channels.

The planet/star contrast ratios of XO-3b are within $[-2.2, 0.3, -0.8, -1.7]$ - σ of the thermal inversion in the upper stratosphere model of XO-3b in the 3.6 micron, 4.5 micron, 5.8 micron, and 8.0 micron channels respectively. The measured planet/star contrast ratios are inconsistent at more than $3\text{-}\sigma$ in the 3.6 micron, 4.5 micron, 5.8 micron, and 8.0 micron channels with the thermally non-inverted upper atmosphere model (dot-dashed line and open circles as band averages in Fig. 5). The flux contrast ratios of XO-3b in the 4 IRAC channels thus represent a detection of an upper atmospheric temperature inversion similar to the temperature-pressure profile depicted as a solid line in Fig. 1. We further note that the XO-3b flux ratios can be reproduced in the 3.6 micron, 4.5 micron, and 5.8 micron channels by a black body with an effective temperature $T_{eff} = 1550$ K as well.

A correlation between minimum insolation at the planet’s substellar point and the presence of stratospheric temperature inversions has been recently emerging (Burrows et al. 2008; Fortney et al. 2008) from numerous Hot-Jupiter spectral energy distribution measurements (Harrington et al. 2007; Charbonneau et al. 2008; Knutson et al. 2008, 2009b; Machalek et al. 2008, 2009; O’Donovan et al. 2009; Fressin et al. 2009; Todorov et al. 2010; Christiansen et al. 2009; Gillon et al. 2009). Currently $F_p \sim 1.0 \times 10^9$ ergs $\text{cm}^{-2} \text{s}^{-1}$ of flux at the planetary substellar point is thought to be necessary for the extra optical absorber to drive a stratospheric temperature inversion, although significant outliers exist: XO-1b with a substellar point flux of $F_p \sim 0.49 \times 10^9$ ergs $\text{cm}^{-2} \text{s}^{-1}$ has a stratospheric temperature inversion (Machalek et al. 2008); while TrES-3 is strongly irradiated and yet possesses no thermal inversion according to Fressin et al. (2009). The planet HAT-P-1b has intermediate subsolar flux between XO-1b and TrES-3 and presents evidence for a weak thermal inversion Todorov et al. (2010). Also, the flux ratios of the planet CoRot-2b ($F_p \sim 1.3 \times 10^9$ ergs $\text{cm}^{-2} \text{s}^{-1}$) in 4.5 micron and 8.0 micron IRAC channels provide a tentative non-detection of thermal inversion (Gillon et al. 2009).

The distance to XO-3 is currently uncertain, so are the estimates for the stellar mass and radius. Therefore the substellar point flux at the XO-3b is estimated to be in the range $F_p \sim (1.9 - 4.2) \times 10^9$ ergs $\text{cm}^{-2} \text{s}^{-1}$, Liu et al. (2008). This entire flux range is well above the threshold value and therefore strongly predictive of a temperature inversion in the strato-

sphere of XO-3b, which is detected in our dataset.

The diagnosis of temperature inversions in Hot Jupiter atmospheres is still somewhat model dependent as exemplified by the color-color diagram of Gillon et al. (2009). This figure shows that although TrES-3b (Fressin et al. 2009) and TrES-2b (O’Donovan et al. 2009) have almost identical colors, an inversion is claimed for TrES-2b but not for TrES-3b. Alternative determinants for the cause of temperature inversions in stratospheres of hot Jupiters have been suggested by Zahnle et al. (2009) in the form of sulfur photochemistry. Furthermore, three dimensional global circulation models (3D GCM) by Showman et al. (2009); Rauscher & Menou (2009) suggest that dynamic weather patterns can induce temperature inversions even without extra stratospheric optical absorbers. Obtaining flux ratios of hot Jupiters with varying degrees of stellar insolation, planetary metallicity, and eccentricity at multiple IR wavelengths with Spitzer IRAC or JWST in the future will help to constrain the cause of stratospheric thermal inversions in hot Jupiters.

4. Conclusion

We determined the flux ratios of the planet heavy and eccentric planet XO-3b to its parent star in the 4 IRAC bands: $0.101\% \pm 0.004\%$ at 3.6 micron; $0.143\% \pm 0.006\%$ at 4.5 micron; $0.134\% \pm 0.049\%$ at 5.8 micron and $0.150\% \pm 0.036\%$ at 8.0 micron. The flux ratios point towards a stratospheric temperature inversion best fit with atmospheric models with a uniform stratospheric absorber of $\kappa_e = 0.2 \text{ cm}^2/\text{g}$.

XO-3b is strongly irradiated with a subsolar point flux $F_p \sim (1.9 - 4.2) \times 10^9 \text{ ergs cm}^{-2} \text{ s}^{-1}$, depending on uncertain parent star parameters and eccentric orbit. This high flux is expected to cause a thermal inversion in the planet’s stratosphere, which is indeed observed. Obtaining the parallax distance Johns-Krull (2008) to the parent star XO-3 would refine both the stellar and planetary masses and radii and hence constrain better the subsolar point flux F_p . The correlation between the presence of a temperature inversion in a hot Jupiter atmosphere and the subsolar point flux from the parent star is insufficient to explain why high insolation planets like TrES-3 do not have stratospheric inversions and some low insolation planets like XO-1b do have inversions. Secondary factors such as sulfur chemistry, atmospheric metallicity, amounts of macroscopic mixing in the stratosphere, or even dynamical weather effects likely play a role.

Using the secondary eclipse timing centroids we refined the orbital eccentricity of XO-3b to be $e = 0.277 \pm 0.009$, which is $1.0\text{-}\sigma$ higher than the radial velocity derived eccentricity $e = 0.260 \pm 0.017$ (Winn et al. 2008; Johns-Krull et al. 2008). The refined eccentricity increases the amount of tidal energy dissipation rate by 29%, and the radius-age trajectories for XO-3b thus imply that at least some amount of tidal-heating must be responsible for the inflated radius of XO-3b. The tidal heating parameter is constrained to $Q_p \lesssim 10^6$. A more accurate radius measurement of XO-3b is needed from a parallax distance to the parent star XO-3 either from the Hubble Space Telescope or the future GAIA mission to further refine its tidal heating rate and the allowable range for the tidal heating parameter Q_p .

The authors would like to thank the anonymous referee for a speedy and thorough review, which has substantially improved the manuscript. The authors would also like to acknowledge the use of publicly available routines by Eric Agol and Levenberg-Marquardt least-squares minimization routine MPFITFUN by Craig Markwardt. P.M. and P.R.M. were supported by the Spitzer Science Center Grant C4030 to the Space Telescope Science Institute and the Bay Area Environmental Research Institute. A.B. was supported in part by NASA grant NNX07AG80G. We also acknowledge support through JPL/Spitzer Agreements 1328092, 1348668, and 1312647. T.G. acknowledges funding by NASA Ames Research Center to the Ames Center for Exoplanet Studies in support of this work. This work is based on observations made with the Spitzer Space Telescope, which is operated by the Jet Propulsion Laboratory, California Institute of Technology under a contract with NASA. This publication also makes use of data products from the Two Micron All Sky Survey, which is a joint project of the University of Massachusetts and the Infrared Processing and Analysis Center/California Institute of Technology, funded by the National Aeronautics and Space Administration and the National Science Foundation.

Table 1. Secondary eclipse best fit parameters for XO-3b

λ (microns)	Eclipse Depth ΔF	Eclipse Center Time (HJD)	Eclipse Center Phase Φ
3.6	$0.101\% \pm 0.004\%$	$2454908.40094 \pm 0.01003$	0.6720 ± 0.0031
4.5	$0.143\% \pm 0.006\%$	$2454943.50512 \pm 0.00608$	0.6712 ± 0.0019
5.8	$0.134\% \pm 0.049\%$	$2454908.40213 \pm 0.01427$	0.6724 ± 0.0045
8.0	$0.150\% \pm 0.036\%$	$2454943.50501 \pm 0.01904$	0.6712 ± 0.0060

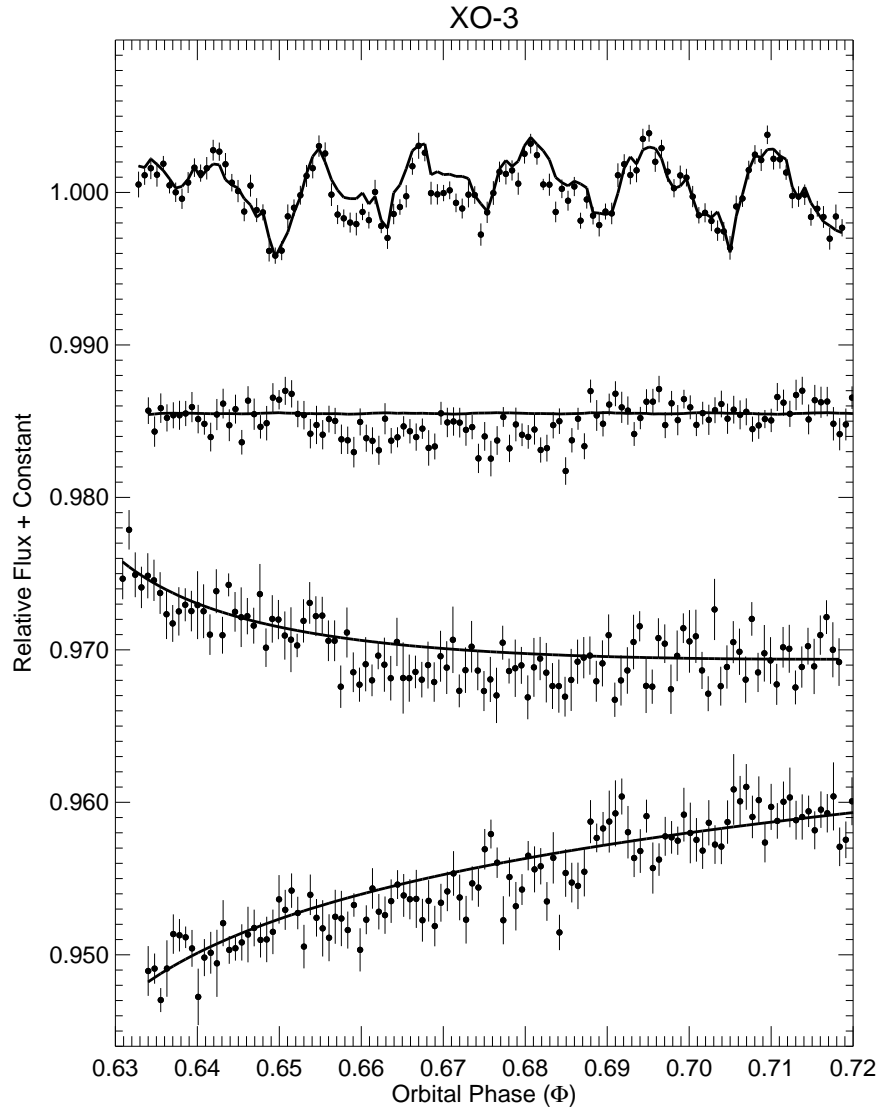


Fig. 3.— (left) Secondary eclipse observations of XO-3 with IRAC on *Spitzer Space Telescope* in 3.6 micron, 4.5 micron, 5.8 micron and 8.0 micron channels (from top to bottom) binned in 3.5-minute intervals and normalized to 1 and offset for clarity. Note, however, that all our analysis is performed on the unbinned data. The overplotted solid lines show the corrections for the detector effects (see text).

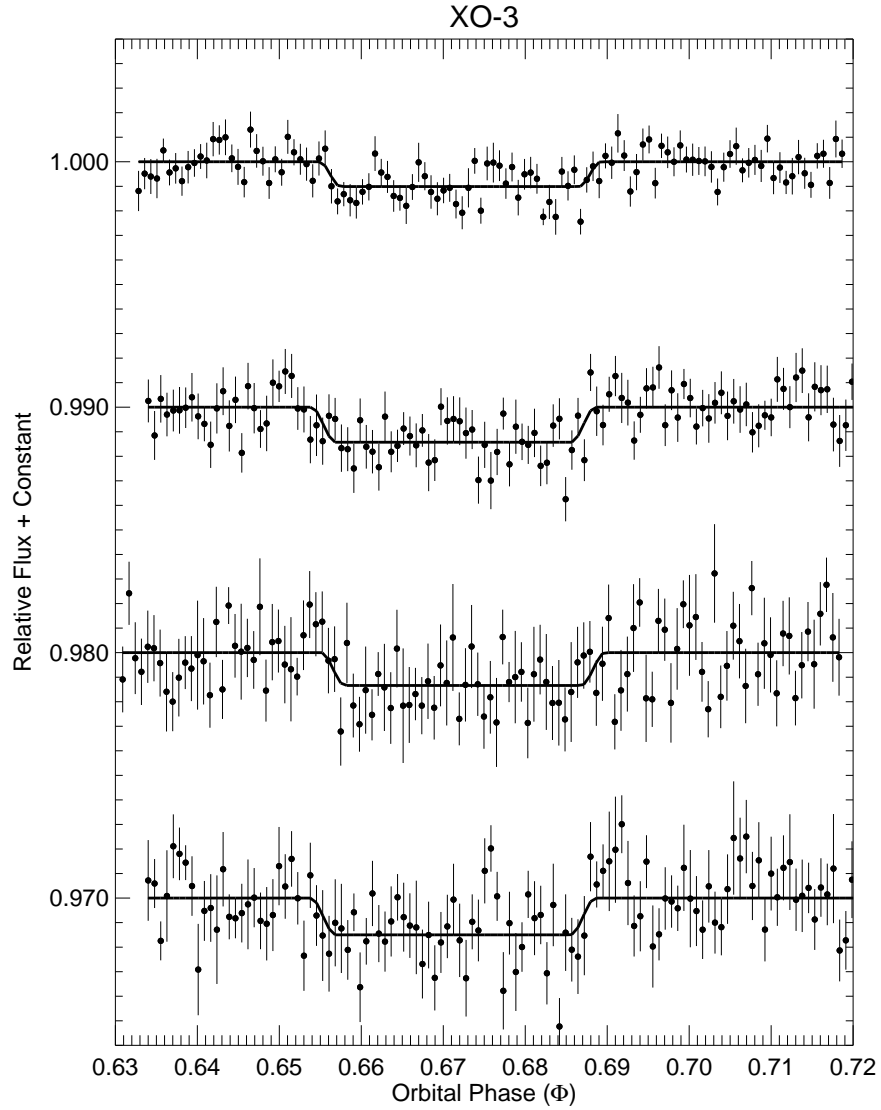


Fig. 4.— Secondary eclipse of XO-3b around the star XO-3 observed with IRAC on *Spitzer Space Telescope* in 3.6, 4.5, 5.8, and 8.0 micron channels (top to bottom) corrected for detector effects, normalized and binned in 3.5-minute intervals and offset for clarity. The best-fit eclipse curves are overplotted. Note, however, that all our analysis is performed on the unbinned data.

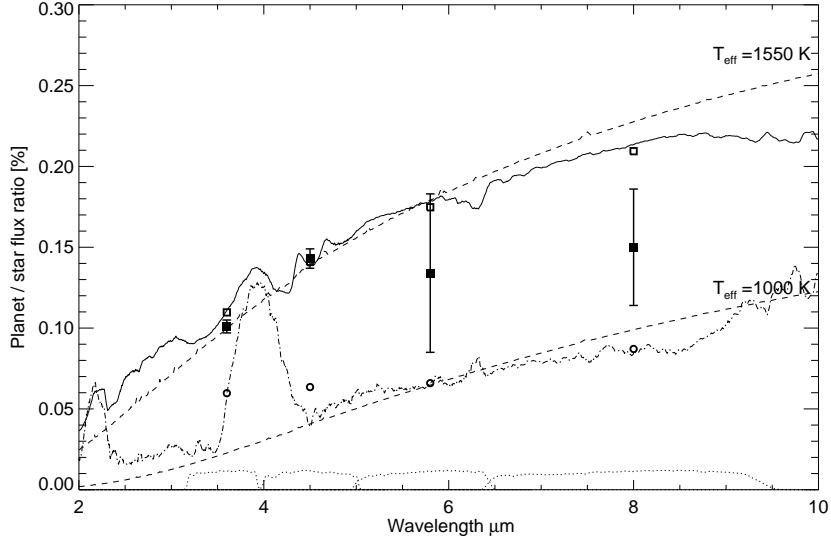


Fig. 5.— *Spitzer Space Telescope* IRAC secondary eclipse depths for XO-3b with MCMC error bars (filled squares). The predicted emission spectrum of the planet (Burrows et al. 2007b, 2008; Spiegel et al. 2009) with an upper atmospheric absorber of $\kappa_e = 0.2 \text{ cm}^2/\text{g}$ and redistribution parameter of $P_n=[0.2]$ is plotted as a solid line. A model with no atmospheric absorber and a redistribution parameters of $P_n=[0.3]$ is over plotted with dot-dashed line (see §3.2 for details). Both model emission spectra are calculated for XO-3b orbital distance $a = 0.0454 \text{ AU}$ (Winn et al. 2008) and stellar insolation $F_p \sim 2.01 \times 10^9 \text{ ergs cm}^{-2} \text{ s}^{-1}$. See §3.2 for more details. The band-averaged flux ratios are plotted as open squares and open circles for the models with and without an extra upper atmospheric absorber, respectively. The theoretical flux ratios obtained from a XO-3 stellar spectrum (from <http://wwwuser.oat.ts.astro.it/castelli/grids/gridp05k2odfnew/fp05t6500g35k2odfnew.dat>) and an assumed black-body spectrum for the planet at [1000, 1550] K are plotted as dashed lines. The normalized *Spitzer Space Telescope* IRAC response curves for the 3.6-, 4.5-, 5.8-, and 8.0 micron channels are plotted at the bottom of the figure (dotted lines).

REFERENCES

- Baraffe, I., Chabrier, G., & Barman, T. 2008, *A&A*, 482, 315
- Bodenheimer, P., Lin, D. N. C., & Mardling, R. A. 2001, *ApJ*, 548, 466
- Bodenheimer, P., Laughlin, G., & Lin, D. N. C. 2003, *ApJ*, 592, 555
- Burrows, A., Hubeny, I., Budaj, J., & Hubbard, W. B. 2007a, *ApJ*, 661, 502
- Burrows, A., Hubeny, I., Budaj, J., Knutson, H. A., & Charbonneau, D. 2007b, *ApJ*, 668, L171
- Burrows, A., Budaj, J., & Hubeny, I. 2008, *ApJ*, 678, 1436
- Chabrier, G., Barman, T., Baraffe, I., Allard, F., & Hauschildt, P. H. 2004, *ApJ*, 603, L53
- Charbonneau, D., et al. 2005, *ApJ*, 626, 523
- Charbonneau, D., Knutson, H. A., Barman, T., Allen, L. E., Mayor, M., Megeath, S. T., Queloz, D., & Udry, S. 2008, *ApJ*, 686, 1341
- Christiansen, J. L., et al. 2009, arXiv:0912.2132
- Deming, D., Seager, S., Richardson, L. J., & Harrington, J. 2005, *Nature*, 434, 740
- Désert, J.-M., Lecavelier des Etangs, A., Hébrard, G., Sing, D. K., Ehrenreich, D., Ferlet, R., & Vidal-Madjar, A. 2009, *ApJ*, 699, 478
- Fazio, G. G. et al. 2004, *ApJS*, 154, 10
- Fortney, J. J., Cooper, C. S., Showman, A. P., Marley, M. S., & Freedman, R. S. 2006, *ApJ*, 652, 746
- Fortney, J. J., Marley, M. S., & Barnes, J. W. 2007, *ApJ*, 659, 1661
- Fortney, J. J., Lodders, K., Marley, M. S., & Freedman, R. S. 2008, *ApJ*, 678, 1419
- Fortney, J. J., & Nettelmann, N. 2009, arXiv:0912.0533
- Fressin, F., Knutson, H. A., Charbonneau, D., O’Donovan, F. T., Burrows, A., Deming, D., & Mandushev, G. 2009, arXiv:0909.5221
- Gillon, M., et al. 2009, arXiv:0911.5087
- Goldreich, P., & Soter, S. 1966, *Icarus*, 5, 375
- Gregory, P. C. 2005, *Bayesian Logical Data Analysis for the Physical Sciences: A Comparative Approach with ‘Mathematica’ Support*. Edited by P. C. Gregory. ISBN 0 521 84150 X (hardback); Cambridge University Press, Cambridge, UK, 2005
- Grillmair, C. J., et al. 2008, *Nature*, 456, 767
- Gu, P.-G., Lin, D. N. C., & Bodenheimer, P. H. 2003, *ApJ*, 588, 509
- Guillot, T., Burrows, A., Hubbard, W. B., Lunine, J. I., & Saumon, D. 1996, *ApJ*, 459, L35
- Harrington, J., Luszcz, S., Seager, S., Deming, D., & Richardson, L. J. 2007, *Nature*, 447, 691
- Hubeny, I., Burrows, A., & Sudarsky, D. 2003, *ApJ*, 594, 1011
- Hébrard, G., et al. 2008, *A&A*, 488, 763
- Ibgui, L., & Burrows, A. 2009, arXiv:0902.3998

- Johns-Krull, C. M., et al. 2008, *ApJ*, 677, 657
- Johns-Krull, C. 2008, HST Proposal, 11706
- Jurić, M., & Tremaine, S. 2008, *ApJ*, 686, 603
- Knutson, H. A., et al. 2007a, *Nature*, 447, 183
- Knutson, H. A., Charbonneau, D., Allen, L. E., Burrows, A., & Megeath, S. T. 2008, *ApJ*, 673, 526
- Knutson, H. A., et al. 2009a, *ApJ*, 690, 822
- Knutson, H. A., Charbonneau, D., Burrows, A., O’Donovan, F. T., & Mandushev, G. 2009b, *ApJ*, 691, 866
- Knutson, H. A., Charbonneau, D., Cowan, N. B., Fortney, J. J., Showman, A. P., Agol, E., & Henry, G. W. 2009c, *ApJ*, 703, 769
- Kopal, Z. 1959, *The International Astrophysics Series*, London: Chapman Hall, 1959,
- Laughlin, G., Deming, D., Langton, J., Kasen, D., Vogt, S., Butler, P., Rivera, E., & Meschiari, S. 2009, *Nature*, 457, 562
- Liu, X., Burrows, A., & Ibgui, L. 2008, *ApJ*, 687, 1191
- Machalek, P., McCullough, P. R., Burke, C. J., Valenti, J. A., Burrows, A., & Hora, J. L. 2008, *ApJ*, 684, 1427
- Machalek, P., McCullough, P. R., Burrows, A., Burke, C. J., Hora, J. L., & Johns-Krull, C. M. 2009, *ApJ*, 701, 514
- Mandel, K., & Agol, E. 2002, *ApJ*, 580, L171
- Markwardt, C. B. 2009, arXiv:0902.2850
- Morales-Calderón, M., et al. 2006, *ApJ*, 653, 1454
- Nagasawa, M., Ida, S., & Bessho, T. 2008, *ApJ*, 678, 498
- O’Donovan, F. T., Charbonneau, D., Harrington, J., Seager, S., Deming, D., & Knutson, H. A. 2009, *IAU Symposium*, 253, 536
- Rauscher, E., & Menou, K. 2009, arXiv:0907.2692
- Showman, A. P., Fortney, J. J., Lian, Y., Marley, M. S., Freedman, R. S., Knutson, H. A., & Charbonneau, D. 2009, *ApJ*, 699, 564
- Spiegel, D. S., Silverio, K., & Burrows, A. 2009, arXiv:0902.3995
- Swain, M. R., Vasisht, G., & Tinetti, G. 2008, *Nature*, 452, 329
- Swain, M. R., Vasisht, G., Tinetti, G., Bouwman, J., Chen, P., Yung, Y., Deming, D., & Deroo, P. 2009, *ApJ*, 690, L114
- Swain, M. R., et al. 2009, *ApJ*, 704, 1616
- Tinetti, G., et al. 2007, *Nature*, 448, 169
- Todorov, K., Deming, D., Harrington, J., Stevenson, K. B., Bowman, W. C., Nymeyer, S., Fortney, J. J., & Bakos, G. A. 2010, *ApJ*, 708, 498
- Winn, J. N., et al. 2008, *ApJ*, 683, 1076
- Winn, J. N., et al. 2009, *ApJ*, 700, 302

Zahnle, K., Marley, M. S., Lodders, K., & Fortney, J. J. 2009, arXiv:0903.1663